ROYAL SOCIETY
OF CHEMISTRY

EDGE ARTICLE

Effect of charge-transfer enhancement on the efficiency and rotary mechanism of an oxindole-based molecular motor†

Daisy R. S. Pooler, [ID] ‡[a] Robin Pierron, [ID] ‡[b] Stefano Crespi, [ID] ‡[a] Romain Costil, [ID] [a] Lukas Pfeifer, [ID] [a] Jérémie Léonard, [ID] *[b] Massimo Olivucci [ID] *[cd] and Ben L. Feringa [ID] *[a]

Harvesting energy and converting it into mechanical motion forms the basis for both natural and artificial molecular motors. Overcrowded alkene-based light-driven rotary motors are powered through sequential photochemical and thermal steps. The thermal helix inversion steps are well characterised and can be manipulated through adjustment of the chemical structure, however, the insights into the photochemical isomerisation steps still remain elusive. Here we report a novel oxindole-based molecular motor featuring pronounced electronic push–pull character and a four-fold increase of the photoisomerization quantum yield in comparison to previous motors of its class. A multidisciplinary approach including synthesis, steady-state and transient absorption spectroscopies, and electronic structure modelling was implemented to elucidate the excited state dynamics and rotary mechanism. We conclude that the charge-transfer character of the excited state diminishes the degree of pyramidalisation at the alkene bond during isomerisation, such that the rotational properties of this oxindole-based motor stand in between the precessional motion of fluorene-based molecular motors and the axial motion of biomimetic photoswitches.

Introduction

The first molecular-level step in vision[1] represents a reference model for the design of functional photo-activated molecules[2–14] often called *photoactuators*: this is the photochemical double-bond isomerisation of the protonated Schiff base of 11-*cis*-retinal (rPSB, see Fig. 1A), the co-factor of the scotopic visual pigment Rhodopsin (Rho). Nature has engineered this paradigmatic process to react quickly (<200 fs)[15] and efficiently (quantum yield $\varphi = 67\%$)[16] to a light stimulus, initiating a cascade of protein conformational changes ultimately resulting in the stimulation of the optic nerve. Such isomerisation

displays two basic mechanistic features. First, only one specific double bond isomerises, *i.e.* $C_{11}=C_{12}$, making the reaction diastereoselective. Second, the reactive process occurs *via* population of the charge-transfer, first singlet (S_1) excited state[9] of rPSB, effectively turning the rotationally locked double bond into a freely rotating single bond.[17] One additional notable feature associated with the Rho light-induced isomerisation is the presence of sub-picosecond to picosecond spectroscopic signatures of the vibrational motion driving the $C_{11}=C_{12}$ twist of rPSB.[18–23] These observations were rationalised by computational chemistry studies which provided a mechanistic description of the photoreaction showing that the Rho quantum yield (QY) is controlled by the precise progression along three rPSB vibrational modes, driven by the topographical features of the potential energy surface (PES) along the isomerisation coordinate.[24–27]

The Rho photoisomerisation inspired the preparation of a plethora of photoactuators to harvest light energy and convert it into mechanical energy at the molecular scale.[28–31] Among those, single-molecules featuring a single exocyclic double-bond and, therefore, undergoing a diastereoselective rPSB-like photochemical E–Z isomerisation, allow a rotor moiety to spin with respect to a stator (see Fig. 1B).[32–35] These systems have been employed to control light-actuated molecular muscles,[36,37] photoresponsive gels,[31,38] and mechanical motion of a macroscopic object in liquid crystal polymers.[39] In particular, recent

[a]*Stratingh Institute for Chemistry, Zernike Institute for Advanced Materials, University of Groningen, Nijenborgh 4, 9747 AG Groningen, The Netherlands. E-mail: b.l.feringa@rug.nl*

[b]*Institut de Physique et Chimie des Matériaux de Strasbourg, Université de Strasbourg, CNRS, UMR 7504, F-67034 Strasbourg, France. E-mail: jeremie.leonard@ipcms.unistra.fr*

[c]*Dipartimento di Biotecnologie, Chimica e Farmacia, Università di Siena, 53100 Siena, Italy. E-mail: massimo.olivucci@unisi.it*

[d]*Chemistry Department, Bowling Green State University, Bowling Green, Ohio 43403, USA. E-mail: molivuc@bgsu.edu*

† Electronic supplementary information (ESI) available. CCDC 2064588. For ESI and crystallographic data in CIF or other electronic format see DOI: 10.1039/d1sc01105g
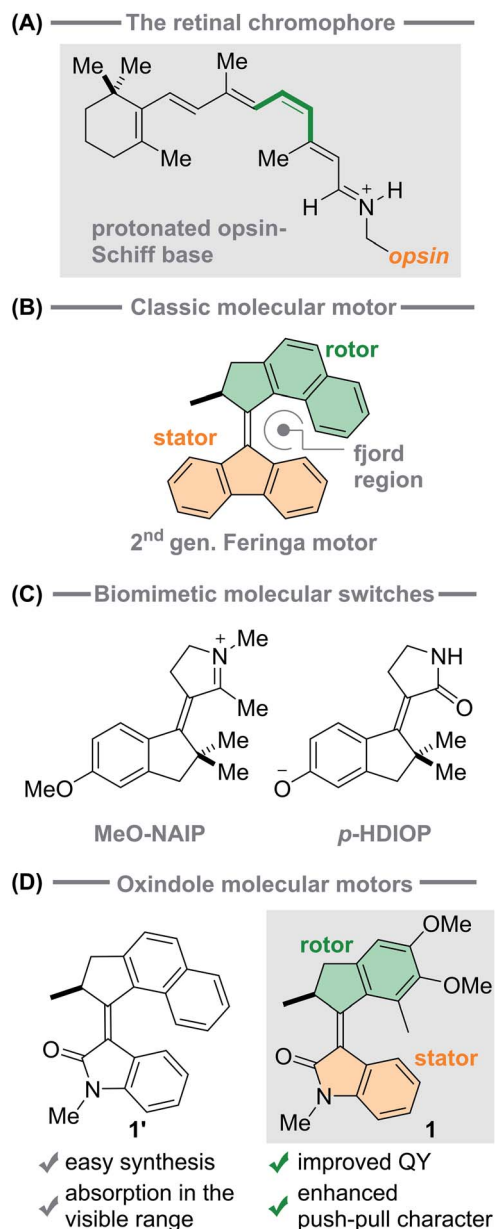
‡ These authors contributed equally.

Fig. 1 (A) Structure of the retinal chromophore. (B) A second generation Feringa motor based on the fluorene scaffold. (C) Biomimetic molecular switches characterised by a charged structure, either positive (MeO-NAIP) or negative (p-HDIOP). (D) Originally reported[52] (1') and novel (1) structures of the oxindole based molecular motor and their characteristic features.

literature reviews the amplification of single molecular motion into macroscopic effects.[2,34,40–43]

While most synthetic photoactuators derive from modifications of well-known cores, *e.g.* azobenzenes, overcrowded alkenes and stiff-stilbenes, other research efforts aimed to more closely mimic the photoisomerisation of Rho. The family of the cationic *N*-alkylated indanylidene-pyrrolinium (NAIP) molecular switches were synthesised to emulate the rPSB π-electron system and S$_1$ charge-transfer character that contributes the unique light-induced dynamics and quantum yield of Rho (see Fig. 1C).[44–49] The design of this system was guided by the

consideration that a precise, mechanistic-level understanding and control on the directionality and properties of the rotational motion generated by the reaction[33] is crucial for the development of effective molecular machines based on double bond isomerisation.

This biomimetic strategy was successful for engineering molecular switches undergoing photoreaction dynamics similar to that of rPSB in Rho,[46] but their photoisomerisation QY does not exceed 35%, and a rational approach remains to be devised for further optimising their efficiency.[48] This strategy was also recently extended to replicate the photochemical isomerisation of the chromophore of the green fluorescent protein in *para*-hydroxydimethylindanylidene-oxopyrroline (*p*-HDIOP) anions (see Fig. 1C), affording more straightforward chemical synthesis.[50,51] Both NAIP cations and *p*-HDIOP anions are characterised by similar electronic structures and PESs, including a *biomimetic* charge-transfer character facilitating the isomerisation *via* S$_1$.[50]

The use of NAIP or *p*-HDIOP scaffolds in unidirectional molecular motors has also been proposed,[53–55] through the incorporation of a stereogenic centre.[56,57]

For a full control of the directionality of the rotational movement generated by the C=C double bond isomerisation, light-driven molecular motors based on chiral overcrowded alkenes (*e.g.* Fig. 1b) operate through sequential excited state photochemical *E–Z* isomerisations and thermal helix inversion (THI) steps.[58] Recently, a novel direction in the quest of advancing unidirectional photoactuators has been pursued by developing molecular motors based on the oxindole core (1', in Fig. 1D).[52] These structures are synthetically accessible through a one-pot Knoevenagel-type condensation and, more interestingly, their rotation can be triggered with visible light, while the dimension of the ring connected to the alkene bond controls the speed of their thermal step.[52] However, it was found that the oxindole-based motors prepared so far have low (2–3%) photoisomerisation quantum yields.

Here, we explore a new version of the oxindole motor enhancing its push–pull (*i.e.* charge-transfer) character to possibly approach an electronic structure and isomerisation mechanism mimicking that of biological chromophores – aiming to improve the photoisomerisation QY – and provide insight into the rotary mechanism. We report the synthesis of the novel motor 1 (see Fig. 1D), and the detailed investigation of its photochemical and thermal steps. We show that 1 preserves the advantageous features of its class,[52] *i.e.* facile synthesis, visible light addressability, fast thermal steps, but also achieves higher quantum yields in the range of 10%. Combined transient absorption spectroscopy and computational studies allow us to reveal its ultrafast photoreaction dynamics and mechanism. In particular, we observe spectroscopic signatures of excited-state vibrational motions driving the system out of the Franck–Condon region, towards a dark state and subsequently to a region comprising a conical intersection (CInt) funnel[9,59] where the decay to the ground state (S$_0$) takes place. These findings are in line with previous observations reported for second-generation Feringa molecular motors.[60]

Concomitant to the observation of the improved QY, the computational investigation of the electronic structure and photoreaction mechanism of **1** concludes that the engineered push–pull character also affects the isomerisation mechanism – which may be categorised as intermediate between the precessional, stilbene-like rotary motion characteristic of the fluorene motors, and the axial, Rho-like rotation typical of the biomimetic molecular switches, as we will discuss below.

Results

Synthesis

Motor **1** was prepared in two steps from commercially available materials (see ESI†). The first step involves a tandem Friedel–Crafts acylation/Nazarov cyclisation of 2,3-dimethoxytoluene and methacrylic acid, facilitated by polyphosphoric acid (PPA). Next, the ketone was subjected to a Knoevenagel condensation with *N*-methyl oxindole, mediated by TiCl$_4$ as a Lewis acid and DBU as a base, yielding motor **1** in 44%, exclusively as the stable *E* isomer (*E*$_S$-**1**). Single crystals suitable for X-ray diffraction were grown from a saturated solution of *E*$_S$-**1** in EtOAc (see ESI†). The structure obtained confirms a C(O)–N bond length of 1.3764(18) Å, which is in line with values for typical oxindole systems,[61] and

a C=C bond of 1.3593(19) Å. Irradiation of a dichloromethane solution of *E*$_S$-**1** (0.01 M) under ambient light at room temperature for 24 h afforded the *Z*$_S$-**1** isomer that could be isolated using flash column chromatography combined with recrystallisation from EtOAc (23% yield). The enantiomers of *E*$_S$-**1** and *Z*$_S$-**1** were separated by HPLC and were irradiated with a 400 nm LED. The CD spectra of the enantiopure samples before and after irradiation show that no racemisation occurs during the photoisomerisation (see ESI†).

Steady-state spectroscopy and assessment of the rotational cycle

The UV-vis spectra in methanol of *E*$_S$-**1** and *Z*$_S$-**1** show a broad absorption band with $\lambda_{max} = 370$ nm ($\varepsilon = 20\ 800$ M^{-1} cm^{-1}) and $\lambda_{max} = 371$ nm ($\varepsilon = 24\ 500$ M^{-1} cm^{-1}), respectively (see Fig. 2). Irradiation at room temperature with either 365 or 390 nm LEDs in methanol afforded in both cases a photostationary state (PSS) composed of a mixture solely consisting of *E*$_S$-**1** and *Z*$_S$-**1** in a 2 : 1 ratio (see Fig. 2A). The absence of metastable states in the photostationary distribution is in line with our previous reports on similar scaffolds[52] and with the simulated spectra of the four species involved in the isomerisation (Fig. 2B). Indeed, the metastable states are predicted to display a marked red-shift
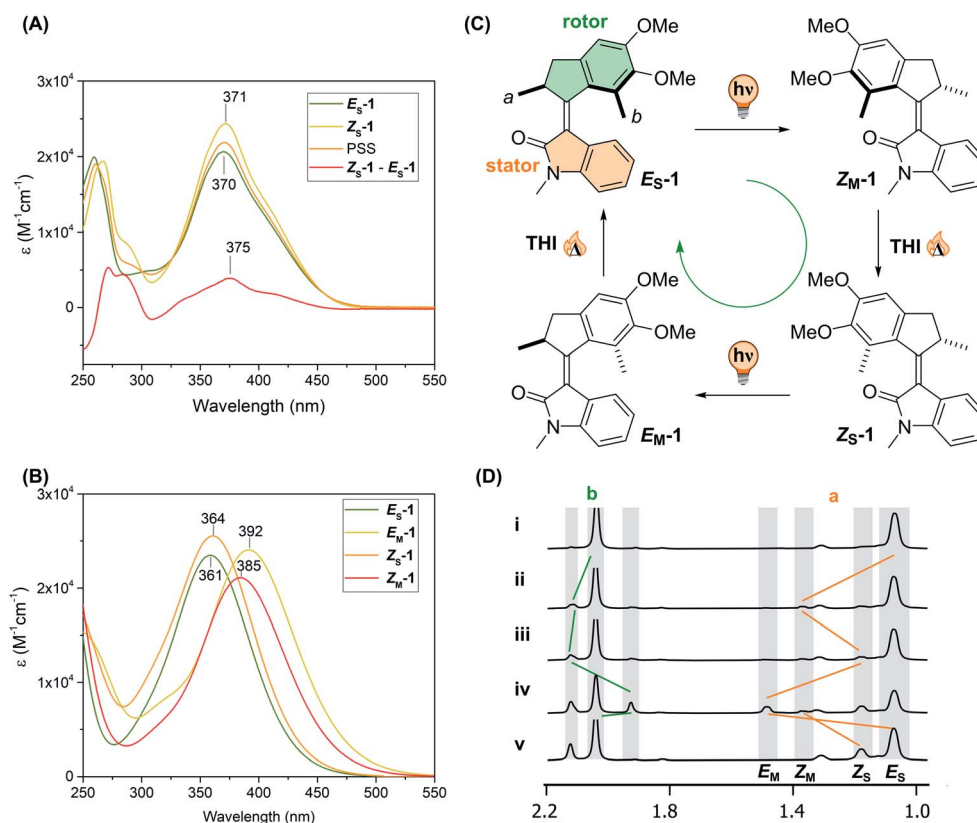

Fig. 2 (A) Steady-state UV-Vis spectra of a 3.8 × 10^{-5} M methanol solution of *Z*$_S$-**1** (yellow), *E*$_S$-**1** (green) – and their difference (red) and photostationary state (PSS, orange) obtained upon 365 nm illumination for two minutes at RT. (B) Simulated absorption spectra and their maxima calculated at the PCM(MeOH)-TD-ωB97X-D/6-311+G(2d,p)//PCM(MeOH)-MP2/6-31G* level of theory for *E*$_S$-**1**, *E*$_M$-**1**, *Z*$_S$-**1** and *Z*$_M$-**1**. (C) Rotation cycle of motor **1**. (D) Selected parts of ^{1}H NMR spectra of *E*$_S$-**1** in CD$_2$Cl$_2$ (3.8 × 10^{-3} M) (i) *E*$_S$-**1** before irradiation; (ii) after 30 min irradiation at 365 nm at −90 °C; (iii) no irradiation, THI, −90 °C, 10 min; (iv) after additional 104 min irradiation at 365 nm at −90 °C (PSS 365 nm); (v) no irradiation, THI, −45 °C, 15 min.

compared to their respective stable forms, a feature not observed in the steady-state UV-vis spectrum of the PSS at room temperature. The photoisomerisation quantum yield of both isomers was measured following either the method of Börjesson and coworkers[62] or the initial slope method[63] (see ESI†). Both methods were in excellent agreement, revealing QY values of 8% to 9% for the E_S-1 and 12% for Z_S-1.

The rotational cycle (Fig. 2C) was first studied by *in situ* irradiation with ^{1}H NMR spectroscopy (Fig. 2D). Upon irradiation of an NMR sample of stable E_S-1 in CD$_2$Cl$_2$ at -90 °C with 365 nm light, a new set of signals appeared, corresponding to the metastable Z isomer (Z_M-1). A significant shift of the methyl group protons at the stereogenic centre (H$_a$), and the protons of the methylene group (H$_{b/b'}$) allowed the detection of this newly formed isomer. The deshielding of H$_a$ is typically observed when the methyl at the stereogenic centre assumes a pseudo-equatorial conformation, which is a fingerprint for the formation of the metastable isomer in Feringa-type motors.[64]

Even at low temperature, Z_M-1 undergoes slow thermal helix inversion (THI) to form the corresponding stable isomer Z_S-1 which can perform a second photoisomerisation to form the metastable E_M-1. Consequently, under continuous irradiation for *ca.* 130 min at -90 °C, the photostationary state (PSS) between all isomers of the motor was obtained. The ratio between the isomers at the PSS$_{365}$ at -90 °C is 61 : 6 : 18 : 15 ($E_S/Z_M/Z_S/E_M$). Raising the temperature (-45 °C, 15 min), E_M-1 undergoes thermal helix inversion, too, to reform E_S-1, completing the 360° rotation and affording the same PSS observed with UV/Vis spectroscopy at room temperature.

The directionality of the motor[52] was confirmed by the sequential appearance of Z_M, Z_S and E_M when irradiating a pure sample of E_S-1 (see Fig. 2D) and when starting the irradiation from Z_S-1 (see Fig. S2, ESI†).

The thermal isomerisation behaviour of 1 was investigated in more detail in CD$_3$OD, following the decay and appearance of new peaks for the protons at the methyl group of the stereogenic centre (H$_a$). A sample of E_S-1 was irradiated with 365 nm and the kinetics of the interconversion of the metastable states back to their relative stable states were followed at temperatures ranging from -90 to -45 °C (see ESI†). Eyring analysis of the decays provided the Gibbs free energy barriers for the thermal steps of the rotation cycle. The metastable Z_M-1 isomer is the most short-lived, with a $\Delta G^\ddagger = 11.8$ kcal mol^{-1}. The corresponding E metastable isomer E_M-1 is slightly more stable, with a $\Delta G^\ddagger = 17.4$ kcal mol^{-1}. The THI energy barriers were also computed at the DFT level of theory with implicit solvation to be between 14.4–15.1 kcal mol^{-1} for Z_M-1, 16.2–16.9 kcal mol^{-1} for E_M-1, reproducing the trend observed experimentally (see Table S3†). These computations also provide information about the transition state structure (see Fig. S53–S56†). In particular, the difference between the two THI barriers comes from the benzylic methyl in the rotor interacting with the C=O in the stator in the Z_M-1 → Z_S-1 transition state or with the bulkier aromatic ring of the oxindole during the E_M-1 → E_S-1 step. (see Fig. 2 and S53–S56†). The free energy barriers for both THI steps of motor 1 are nearly identical to those found for the structurally related oxindole motor previously reported (1′ in Fig. 1).[52]

Hence, the electron-donating MeO substitutions do not affect the THI steps.

Transient absorption spectroscopy

Fig. 3 displays a selection of transient absorption (TA) spectra recorded upon 400 nm excitation of a methanol solution of E_S-1 into S$_1$. About 80 fs after excitation, the early S$_1$ signature is characterised by two excited state absorption (ESA, S$_1$ → S$_n$ transitions) bands peaking at around 455 nm (Vis ESA) and 325 nm (UV ESA). A stimulated emission (SE, S$_1$ → S$_0$ transition) band is also observed as a weak, negative signal at $\lambda >$ 625 nm. The ground state bleach (GSB, S$_0$ → S$_1$ transition) appears around 375 nm. Within the first 270 fs (Fig. 3, top panel), the intensities of the GSB and UV ESA bands increase, which is due to the dynamic blue shift of the positive UV ESA band spectrally overlapping the negative GSB band, most likely characterising the early motion of the S$_1$ population away from the Franck Condon (FC) region. On the same time scale, the Vis ESA and the red SE bands slightly weaken and red-shift. Between 270 fs and 440 fs (Fig. 3, middle panel), no GSB recovery – hence no decay to S$_0$ – is observed, while the UV ESA intensity starts decreasing and the SE completely decays or further red-shifts outside of the observation window. This observation indicates further evolution on the S$_1$ PES, towards conformations of lower S$_1$–S$_0$ oscillator strength and lower S$_1$–S$_0$ energy gaps.
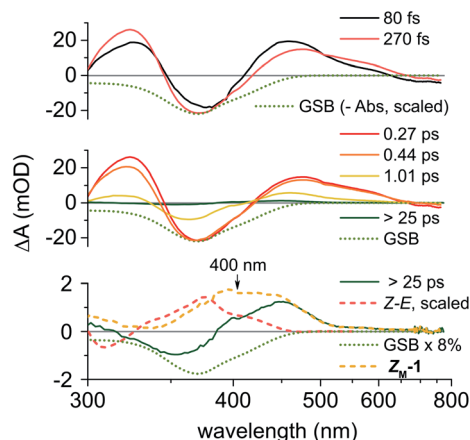

Fig. 3 Selected transient absorption (TA) spectra recorded on E_S-1 in methanol upon 400 nm excitation. Top panel: early pump–probe delays (in fs), up to 270 fs. Middle panel: later delays from 270 fs onwards. In both panels the green dotted line represents the negative, ground state bleach signal as inferred from the scaled steady state absorption of E_S-1. Bottom panel: quasistationary TA spectrum reached after 25 ps (dark green) compared with the difference between the Z_S-1 and E_S-1 steady-state absorption spectra (red dashed line). The GSB contribution in the >25 ps spectrum (green dotted line) is estimated to be ~8% of what it is in the early TA spectra. The absorption spectrum of the photoproduct – assigned to Z_M-1– is computed as the difference between dark green and dotted green lines. Its absorption maximum is ~400 nm (note that some pump light scattering slightly distorts the measured TA spectra at this very wavelength).

Then, by 1 ps all the S_1 signatures and the GSB have decayed significantly, indicating S_1 to S_0 decay. Further spectral relaxation, attributed to vibrational cooling in S_0, occurs until a quasistationary spectrum is reached by 25 ps (weak amplitude, see green line in the bottom panel of Fig. 3), which remains unchanged until the maximum delay of 5 ns achievable in this pump-probe experiment. The >25 ps spectrum does not overlap with the Z–E difference of steady-state spectra (displayed in Fig. 2A), demonstrating that the state formed upon the decay to S_0 is not Z_S-1. The latter must be formed subsequently on a time scale longer than 5 ns. The >25 ps TA spectrum is composed of a positive photoproduct absorption band in the visible range, and a negative, residual GSB, corresponding to 8% of the initial GSB amplitude. By subtracting this GSB contribution from the >25 ps spectrum, we infer the photoproduct absorption spectrum (Fig. 3, yellow dashed line in bottom panel) with maximum around 400 nm. We assign it to the metastable Z_M-1 conformer, formed upon C=C double bond isomerisation of the photoexcited E_S-1 with an estimated 8% photoisomerisation quantum yield, in agreement with the QY values measured independently, as described above.

TD-DFT calculations predict that the UV-Vis absorption maximum for Z_M-1 is 31 nm red-shifted compared to E_S-1 (see Fig. 2B and S57–S58†), consistently with the Z_M-1 spectrum extrapolated here from TA data (Fig. 3, bottom panel). In related oxindole motors featuring higher THI energy barriers,[52] the absorption spectra of their long-lived metastable species could be measured by steady-state spectroscopy and displayed similar spectral shifts with respect to the stable species, in line with the present results.

The TA data recorded with a methanol solution of Z_S-1 under the same conditions are displayed in the ESI Fig. S26† and reveal nearly identical signatures, with a slightly slower blue-shift of the UV ESA and red-shift of the SE up to ~360 fs after excitation. For Z_S-1, the GSB does not start recovering before 0.6 ps, and significant S_1 decay is observed at slightly later delays compared to E_S-1. A quasistationary spectrum is also reached after 25 ps, and interpreted as the superposition of the photoproduct – i.e. the metastable E_M-1 – absorption, peaking close to 400 nm, and a residual GSB contribution evaluated to ~10% of the early (<0.6 ps) GSB amplitude, therefore indicative of a 10% photoisomerisation QY, consistent with the 12% value reported above, and with the Z_S-1 and E_M-1 spectra predicted by TD-DFT calculations (Fig. S59 and S60†).

For both isomers, the early ESA and SE spectral shifts and the lack of GSB recovery reveal S_1 population dynamics illustrated in Fig. 4 with a selection of TA kinetic traces. In both cases, the TA signal rises the fastest (close to the experimental time resolution of ~60 fs) at 460 nm (yellow traces), corresponding to the maximum of the early Vis ESA. The UV ESA traces (black) have a slower rise time and reach their maxima at 270 fs and 360 fs for E_S-1 and Z_S-1, respectively. On the same time scale, the (very weak) SE signals (red dashed traces) already decay. The low-energy side of the Vis ESA bands monitored at 570 nm in Fig. 4 show the slowest rise times reaching their maxima at 415 fs and ~550 fs for E_S-1 and Z_S-1, respectively. At these time
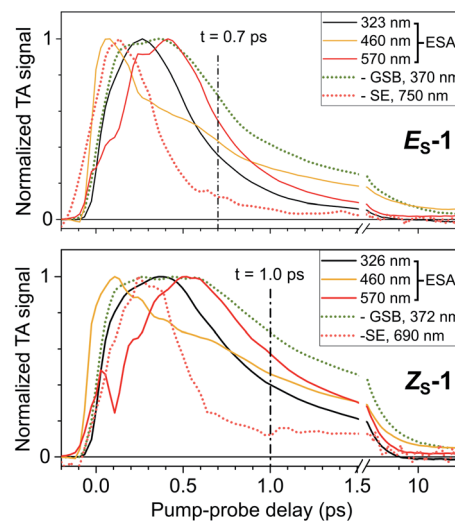

Fig. 4 Comparison of selected, normalised kinetic traces for methanol solutions of E_S-1 (top panel) and Z_S-1 (bottom panel). The kinetics of the UV ESA is illustrated at its absorption maximum of 323 nm (E_S-1) or 326 nm (Z_S-1). The Vis ESA kinetics are monitored at 460 nm (absorption maximum) and 570 nm (low-energy side). The GSB and SE kinetics are monitored by plotting the opposite of the negative signals observed at 370 nm (E_S-1) or 372 nm (Z_S-1), and 750 nm (E_S-1) or 690 nm (Z_S-1), respectively, to facilitate comparison with the other kinetic traces.

delays, the SE signal has already decayed by 80–90%, while the GSB barely starts recovering in both isomers. Altogether, this suggests that within 400 fs (E_S-1) to 600 fs (Z_S-1) – which are also typical time scales for solvent relaxation[65] – the S_1 population evolves to a region of the S_1 PES characterised by a red-shifted and weak $S_1 \rightarrow S_0$ optical transition (vanishing SE), a blue-shifted UV ESA and a red-shifted Vis ESA which both remain relatively intense (transitions from S_1 to higher-lying states). This is reminiscent of the transient, so-called *dark*, excited state already reported for related fluorene molecular motors.[60] Hence, the S_1 lifetime may be estimated from the decay kinetics of the ESA signals. However, no mulitexponential functional form can be used to fit the beginning (first ps) of the observed decay kinetics (see Fig. S25†). This sometimes occurs when electronic populations evolve on time scales faster than vibrational relaxation, in which case rate equation models do not apply (see e.g.[66]). We instead propose to evaluate the S_1 lifetime by specifying the Vis ESA signal half-life, which is in the order of 0.6–0.7 ps for E_S-1 and 0.9–1 ps for Z_S-1 (see black vertical dashed lines in Fig. 4).

Fig. S27† displays the TA spectroscopy data of E_S-1 in nonpolar *n*-hexane. The observations are very similar to those made in polar methanol. Hence, the early spectral relaxations result from S_1 conformational change – rather than solvation dynamics – resulting in a transient, *dark* S_1 species characterised by a vanishing SE, a red-shifted Vis ESA with an almost identical half-life of 0.5–0.6 ps. A quasistationary spectrum is also reached by 25 ps, revealing the Z_M-1 spectrum characterised by two absorption maxima peaking at 380 nm and 440 nm in *n*-hexane (see Fig. S27†).

Notably, the oscillations observed in the Vis ESA band (at 460 nm and 570 nm in Fig. 4, most pronounced in the Z_S-1 case) are indicative of vibrational motion in S_1 away from the FC region during the first 0.5 ps. Fig. 5 illustrates these oscillatory signals in the case of Z_S-1 in methanol and their quantitative analysis, performed with Linear Prediction and Singular Value Decomposition (LPSVD).[67,68] An oscillatory component is clearly observed at 215 ± 8 cm^{-1} with a signal-to-noise ratio of ~5 (see Fig. 5C), and a π phase shift (see black vertical dashed line, in Fig. 5B) in the red side with respect to the blue side of the Vis ESA signature of S_1 (see further discussion in the ESI, Section 8†). In the case of E_S-1, characterised by slightly faster S_1 dynamics (faster ESA red-shift and shorter ESA half-life), similar S_1 oscillations are observed – only in the red side of the Vis ESA band, *i.e.* $\lambda > 500$ nm – at frequencies of 190 ± 10 cm^{-1} in

methanol and 185 ± 12 cm^{-1} in *n*-hexane (see the ESI Fig. S28, S29 and Table S2†).

Excited-state electronic structure modelling

The topography of the PES of **1** was studied at the SA4-XMS-CASPT2/6-31G*//SA3-CASSCF(12,12)/6-31G* level (see ESI†) following a relaxed scan along the rotation coordinate identified by the dihedral angle $C_A C_B C_C C_D$ (see Fig. 6A). More specifically, to account for the missing dynamic electron correlation energy at the SA3-CASSCF(12,12)/6-31G* level of theory employed to follow the S_1 relaxation, the energy is re-evaluated *via* multistate multi-configurational second-order perturbation theory through single point SA4-XMS-CASPT2 computations.

While this protocol represents, arguably, the most robust excited state calculation that can be afforded for the system under investigation, the results remain semi-quantitative due to the different level of theory used for the geometry and energy calculations as well as for the use of a basis set of a limited size. The electronic structures computed for both isomers are very similar, hence we report here on the results for the E isomer and refer to the ESI (Section 9†) for the Z isomer.

The computed $S_0 \rightarrow S_1$ transition of E_S-1 is allowed with an oscillator strength $f = 0.13$, while the $S_0 \rightarrow S_2$ transition is much weaker with $f = 3.9 \times 10^{-3}$. TD-DFT at the PCM(MeOH)-TD-ωB97X-D/6-311+G(2d,p)//MP2/6-31G(d) level shows the same trend, corroborating the hypothesis that S_1 is the state populated directly after the photoexcitation. TD-DFT affords slightly higher oscillator strengths for both $S_0 \rightarrow S_1$ and $S_0 \rightarrow S_2$ ($f = 0.56$ and 0.15, respectively), due to the different type of limitations associated to these quantum chemical approaches (see ESI†).

At the CASSCF level of theory, we identify an S_1 energy minimum (E_S-1_{FC}) in a flat region lying near the Franck–Condon (FC) point and characterised by a locally excited – rather than a charge-transfer – electronic character. Indeed, E_S-1_{FC} shows a very limited charge separation with the stator accommodating a Mulliken charge of +0.16, *versus* +0.17 at the same geometry in S_0 (see ESI†). E_S-1_{FC} is predicted to be optically bright, with the same oscillator strength $f = 0.13$ for emission, as computed for ground state absorption. We propose that the observed SE in the TA experiments (see Fig. 5) originates from this region of the S_1 PES.

The initial S_1 movement from the Franck–Condon point to E_S-1_{FC} follows a rocking motion of the rotor (see ESI animated figure†). After calculation of the vibrational frequencies of the stationary E_S-1_{FC} point, we identified a specific mode, ν_{16} at 200 cm^{-1}, which best corresponds to the aforementioned deformation (see ESI animated figure†). Hence, we assign the oscillatory signals observed in the Vis ESA band to this mode (see ESI† for a more detailed discussion). The same conclusions hold for the other isomer, where the ν_{16} mode characterising the stationary point Z_S-1_{FC} is predicted at 210 cm^{-1}, in line with the slightly higher frequency observed for the oscillatory TA signals of Z-1. We note that prominent S_1 vibrational activity was already reported in *cis*-stilbene[69] at 216 cm^{-1}, in *cis*-stiff-stilbene at 194 cm^{-1},[70] and in molecular motors at somewhat lower frequencies.[60,71]
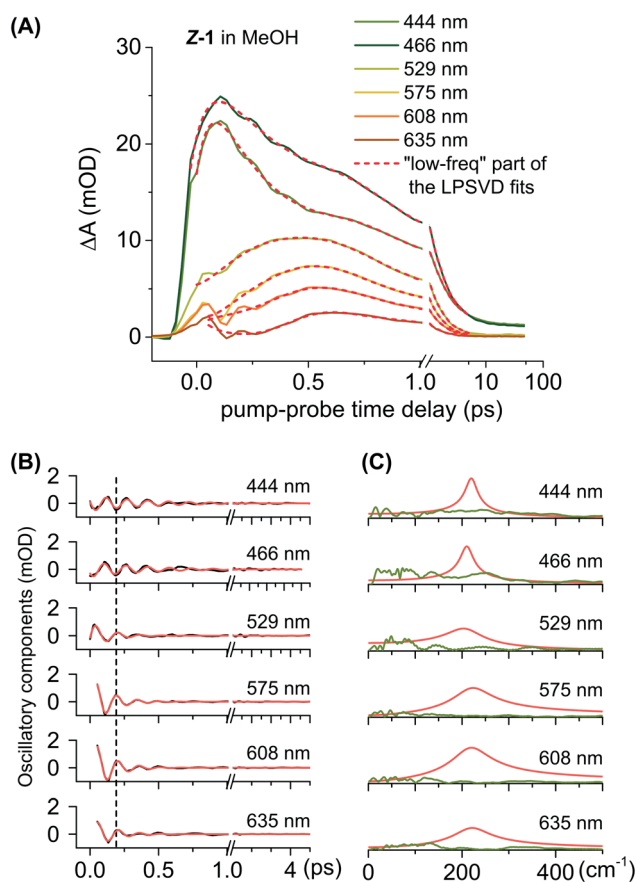

Fig. 5 LPSVD analysis of the Vis ESA kinetic traces of Z_S-1 in methanol, evidencing signatures of vibrational coherent motion in S_1. (A) Selection of TA kinetic traces recorded in the high-energy side (<500 nm) and low-energy side (>500 nm) of the Vis ESA band. The red dotted lines are reconstructed including only the low-frequency components – *i.e.* <100 cm^{-1} – of the LPSVD fit of the kinetics traces. (B) The oscillatory part of the TA signal (black lines, computed as the difference between the TA kinetics and the red dotted curves in panel A) are compared with the high-frequency part (>100 cm^{-1} only, red curves) of the LPSVD fit. (C) LPSVD spectrum (red) of the red traces in panel B, compared with the Fourier transform (FFT, green) of the residuals of the LPSVD fit. The spectral amplitude associated with the prominent vibrational mode at ~215 cm^{-1} is about 3 to 10 times larger than the average spectral amplitude of the fit residuals.
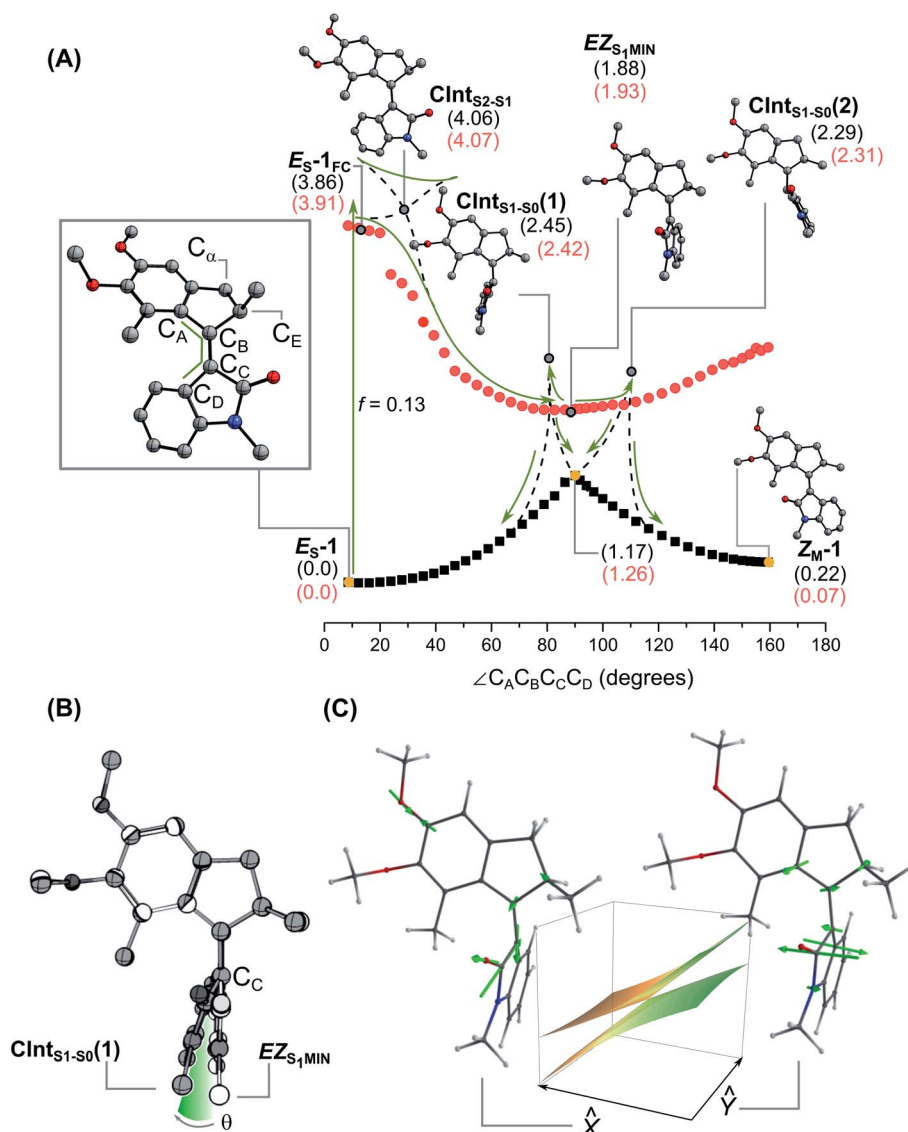
Fig. 6 Excited state isomerisation of E_S-1. (A) Optimised S_0 and S_1 profiles along the rotation coordinate identified by the $C_A C_B C_C C_D$ dihedral angle at the XMS-CASPT2/6-31G*//CASSCF(12,12)/6-31G* level of theory. The relative energies in eV of the stationary points and CInts found along the relaxed scan are reported in parentheses (black: gas phase; red: single point using the PCM model for methanol). (B) Superposition of the geometry of $EZ_{S1\text{-}MIN}$ (in white) and $CInt_{S1\text{-}S0}(1)$ (in grey). The two structures mainly differ for their degree of pyramidalisation ($\angle \theta$) of C_C of the lower half. (C) Depiction of the branching plane of $CInt_{S1\text{-}S2}(1)$ with the vectors $\hat{x}$ and $\hat{y}$ highlighted. Vector $\hat{x}$ features the pyramidalisation distortion typical of the alkene branching plane, while vector $\hat{y}$ describes the $C_B = C_C$ bond twisting associated with the rotation. The sloped nature of the CInt can be appreciated by the tilting in the $\hat{x}$ direction.

Progression along the double bond isomerisation coordinate leads towards the region of a CInt with the S_2 state ($CInt_{S2\text{-}S1}$; see Fig. 6A and B). At higher values of $\angle C_A C_B C_C C_D$ dihedral angle, the PES has a steep decrease in energy, resulting in a sloped path towards a global S_1 minimum at *ca.* 90° (45.5 kcal mol^{-1} downhill compared to E_S-1_{FC} at the XMS-CASPT2 level; all the energies described in the following paragraphs are from the same level of theory), that we label $EZ_{S1\text{-}MIN}$ and refer to as the *perpendicular* state in the following discussion. $EZ_{S1\text{-}MIN}$ features a substantially planarised oxindole ring, with no pyramidalisation in C_B or C_C either ($\theta = 1°$, see Fig. 6B). More accurate energy evaluation at the XMS-CASPT2 level shifts $CInt_{S2\text{-}S1}$ to higher energies, replacing it

with a sloped avoided crossing. Such a refined topography does however not change the general reaction mechanism. In particular, both levels of theory predict a qualitative change in electronic character at the (avoiding) crossing with the negative charge on the stator increasing progressively from +0.16 Mulliken units at E_S-1_{FC} to −0.66 at $EZ_{S1\text{-}MIN}$.

Hence, the perpendicular state displays a zwitterionic character due to an almost complete charge transfer between stator and rotor. Finally, we notice that $EZ_{S1\text{-}MIN}$ is characterised by an extremely weak S_1 to S_0 oscillator strength ($f = 6.3 \ 10^{-4}$), which makes it optically dim.

Two CInts ($CInt_{S1\text{-}S0}(1)$ and $CInt_{S1\text{-}S0}(2)$) connect S_1 and S_0 (see Fig. 6). Compared to $EZ_{S1\text{-}MIN}$ these funnels are

energetically uphill by +13.0 and +9.3 kcal mol^{-1}, and slightly more pyramidalised, with $\theta = 13°$ and 12° for $CInt_{S1-S0}(1)$ and $CInt_{S1-S0}(2)$, respectively (see Fig. 6B and ESI†). Both CInts have an even stronger charge-transfer character, with an almost unitary negative charge delocalised on the stator (−0.91 Mulliken units for $CInt_{S1-S0}(1)$ and −0.93 for $CInt_{S1-S0}(2)$). Interestingly, the addition of an implicit solvent contribution (MeOH using the PCM method, see red values in Fig. 6A), has only a limited effect on the relative energies of the excited state species, while stabilising more effectively the metastable species at the ground state. While it overlooks explicit hydrogen bonding between solvent and solute, this evaluation of the MeOH solvent effect is simplistic but already in line with the observed similarity of the photoreaction dynamics in MeOH and n-hexane. We note, that a similar lack of solvent polarity effect was previously reported in Feringa motors.[72,73]

The branching space vectors[74] $\hat{x}$ and $\hat{y}$ (*i.e.* the *ortho*-normalised g and h branching plane vectors) are displayed in Fig. 6C for $CInt_{S1-S0}(1)$. They reveal the nature of motions which lift the CInt's degeneracies, and therefore govern the excited state decay mechanism. For both CInts, vector $\hat{y}$ describes the $C_B=C_C$ bond twisting associated with the reaction coordinate. In contrast, vector $\hat{x}$ features the pyramidalisation distortion typical of the alkene branching plane,[75] as well as a bond-length alternation (BLA) component typical instead of the Rho branching plane. Notably, in addition to the central $C_B=C_C$ double stretching, the BLA component involves a substantial stretching of the Ar–OMe and C=O bonds (see also the animated figures in ESI†), showcasing the influence of the push–pull system on the CInt topography. As we will discuss below, these results suggest that the character of the branching plane motions lies in between the two limiting cases of *twist-pyramidalisation* and *twist-BLA* previously associated to stilbene-like and Rho-like isomerisation mechanisms, respectively.[33]

It is also worth mentioning that, given the sloped topography of the $CInt_{S1-S0}$, the decay would actually occur in the region extending from the conical intersection towards the orthogonal intermediate EZ_{S1-MIN}. Notice that, if this is the case, then the decay "funnel" would feature a further diminished pyramidalization with respect to the $CInt_{S1-S0}$.

Discussion

As compared to the previously reported oxindole motors,[52] **1** carries two electron-rich methoxy substituents allowing us to fine tune the electronic structure of the motor. Tuning of the S_1 electronic structure and photoreaction properties of neutral stilbenoid molecular motors was already explored *via* introducing electron-donating or electron-withdrawing substituents.[76]

In particular, the grafting of an electron-poor CN group on the rotor moiety improved the isomerisation QY up to 20% for a 2nd generation Feringa-type motor also characterized by a longer-lived (∼10 ps) S_1 *dark* state proposed to feature enhanced pyramidalization.[72,77] Here, we observe that the isomerisation QY of **1** increases four-fold compared to the originally reported oxindoles (QYs *ca.* 2–3%). Besides, owing to the inherent structural resemblance of biomimetic *p*-HDIOP

switches and 2nd generation oxindole-based molecular motors, we aim to explore whether the enhanced push–pull character of **1** allows us to approach an S_1 electronic structure and photo-reaction mechanism mimicking that of biological chromophores – with the expectation that it will help to guide and rationalise the chemical synthetic design of molecular motors showing further QY enhancement. First, we recall that distinct CInt electronic structures and topographies lead to qualitatively distinct mechanistic pictures.[33]

Stilbenoid molecular motors and the corresponding parent stilbene are neutral in their ground state but acquire a charge-transfer – or zwitterionic – character in their S_1 perpendicular (*e.g.* EZ_{S1-MIN}) state.[75] More precisely, in transient structures of this minimum, the isomerising bond acquires local polarisation with one of the two C atoms of the olefinic bond carrying significant negative partial charge and therefore acquiring a pronounced pyramidalisation distortion (see angle θ in Fig. 7C), especially at the CInt. The mechanistic consequences are the following: (i) the branching plane vectors associated to the $S_1 \rightarrow S_0$ CInt, featuring degenerate diradical/charge-transfer characters, describe the so-called *twist-pyramidalisation* motion (see Fig. 7A), (ii) the path going from the low energy region of the S_1 PES to the CInt is dominated by a charge-transfer electronic character and (iii) the motion leading towards the CInt and therefore molecular-scale rotary motion is precessional (see Fig. 7B).[33] Conversely, in Rho and biomimetic switches, (i) the branching plane vectors associated to the same type of $S_1 \rightarrow S_0$ CInt describe a so-called *twist-BLA* (see Fig. 7A), (ii) the path going from the low energy region of the S_1 PES to the CInt is dominated by a mixed diradical-zwitterionic character, but displaying a much more pronounced charge translocation with respect to the one occurring upon excitation to the FC state,[17,50] and (iii) no pyramidalisation occurs, the rotary motion becomes purely axial (see Fig. 7B).[33]

The combined experimental and computational investigation reported above allows us to sum up the photoreaction dynamics of **1** as follows. We observe that electronic excitation to S_1 triggers a fast isomerisation around the unlocked stilbenoid C=C double bond, with S_1 lifetimes in the 1 ps range, like for the unsubstituted fluorene motor of Fig. 1B.[60,72]

More precisely, the initially bright, locally-excited S_1 state evolves within 400 to 600 fs into a transient S_1 state where SE is no longer present. This early S_1 evolution is accompanied by an oscillatory behaviour observed in the Vis ESA for both isomers. We tentatively ascribe this vibration to the excited state ν_{16} mode which best corresponds to the conformational deformation from the initial Franck–Condon point to the nearby local minimum of the bright region.

XMS-CASPT2//CASSCF calculations suggest an almost barrierless evolution in the vicinity of $CInt_{S2-S1}$ connecting the initial locally-excited and bright FC state to a region of the S_1 PES featuring a strong charge-transfer character between the rotor and stator halves. This region presents a global minimum characterised by a perpendicular arrangement of the alkene bond (see Fig. 7) and a low S_1 to S_0 oscillator strength. Hence, we assign the SE decay and ESA spectral shifts – observed in the first 400 to 600 fs – to the formation of this *perpendicular* state,
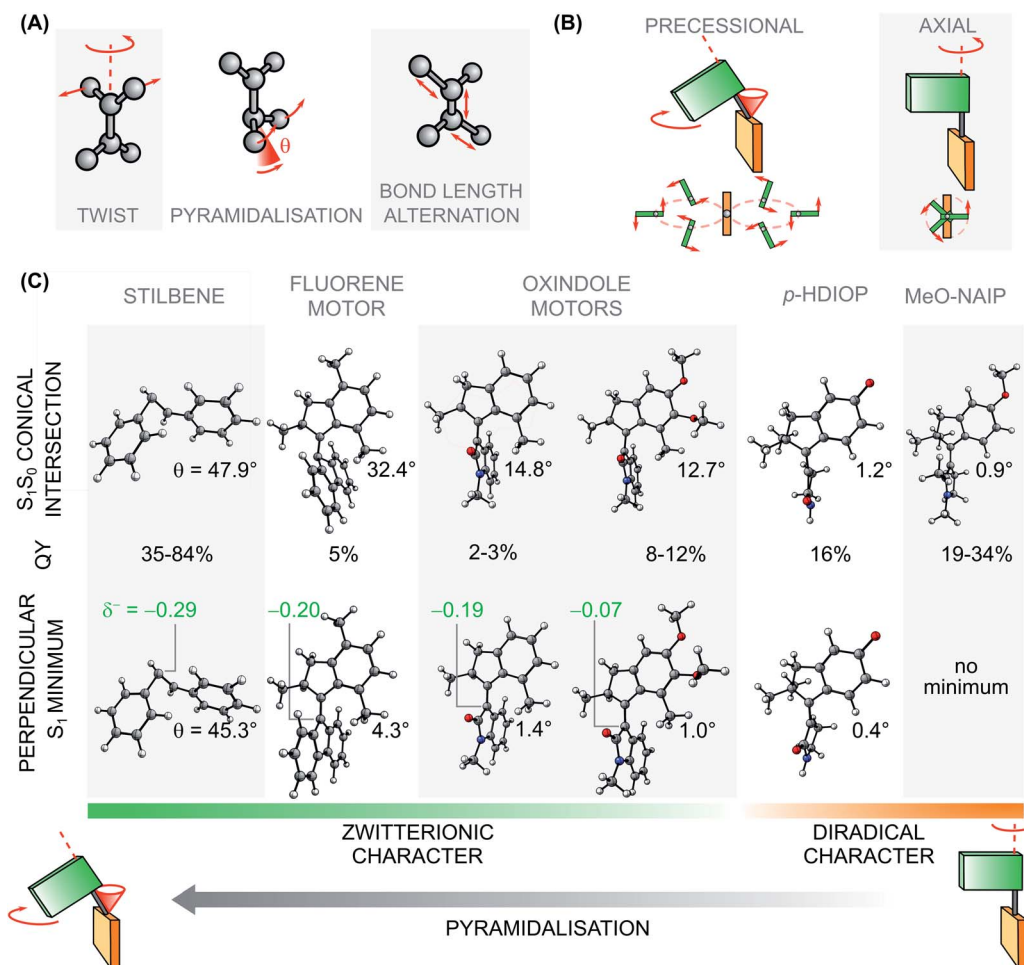
Fig. 7 Mechanistic features of the rotation. (A) Modes associated to the excited state rotational movement of overcrowded alkenes and Rho-like compounds. (B) Paradigmatic rotational motions: on the left the precessional (or hippopede-like) type, typical of switches and motors with zwitterionic character around the S_1 global minimum/$S_1 \rightarrow S_0$ CInt; on the right the axial type, typical of photoactuators with diradical character at the S_1 global minimum/$S_1 \rightarrow S_0$ CInt.[33] (C) QYs of isomerisation and pyramidalisation (θ, in degrees) of the perpendicular (phantom or dark) state and selected $S_1 \rightarrow S_0$ CInts for different photoactuators characterised by zwitterionic (i.e. charge-transfer) or diradical character. The Löwdin charge (δ^-) at the at the pyramidalised carbon of the perpendicular, zwitterionic S_1 minimum of the motor was calculated at the SF-BH&HLYP/cc-pVDZ level on the optimised geometries present in the literature.[72,78,79] The unsubstituted oxindole motor was optimized at the CASSCF(12,12)/6-31G* level of theory, with an active space comparable to the one used for 1. It has to be noted that MeO-NAIP does not present a minimum distinct from the CInt.

reminiscent of the *phantom* state described in the isomerisation of stilbene derivatives[80,81] and of the *dark state* in molecular motors.[60,82] However, despite its pronounced charge-transfer character the *perpendicular* state of 1 does not display the highly pyramidalised carbon expected for such states.[75,83] Instead, EZ_{S1-MIN} features a substantially planarised oxindole ring and C_B atom and its pyramidalisation angle at C_C is only $\theta = 1°$ whereas it is $\theta = 45°$ for stilbene (see Fig. 7C).[75]

After reaching the S_1 perpendicular state, 1 decays to S_0 in the region of two sloped CInts, eventually populating the metastable isomer of the opposite configuration. When comparing $CInt_{S1-S0}(1)$ and $CInt_{S1-S0}(2)$ to the analogous CInt of stilbene and stilbenoid photoactuators, it is apparent that the degree of pyramidalisation at C_C is strongly diminished ($\theta = 12–13°$) with respect to the related carbon ($\theta = 48°$) in stilbene[75] and in a fluorene motor ($\theta = 32–35°$).[79] Comparably, the

unsubstituted oxindole motor possesses a very similar pyramidalisation in the minimum ($\theta = 1.4$) and in the CInt ($\theta = 14–16°$) compared to 1. We argue that the diminished pyramidalisation of the *perpendicular* minimum and related CInts of the oxindole motors is the consequence of the presence of the amide group. However, the enhanced push–pull effect of two methoxy substituents in compound 1 favours even more the delocalisation of the negative charge on the ring, as suggested by the comparison of the partial charge δ^- residing on the pyramidalised carbon in the different photoactuators featuring a zwitterionic perpendicular S_1 minimum (see Fig. 7C).

Altogether, we propose that due to the reduced pyramidalisation and enhanced BLA contribution of the branching plane motions, the actual rotary motion of 1 must be intermediate between the precessional movement of fluorene motors[33] or

stilbene,[75] and the axial rotation expected for non-pyramidalised – *e.g.* biomimetic (NAIPs or *p*-HDIOP) – compounds (see Fig. 7).[50]

For the paradigmatic example of the Rho photoreaction, a detailed description of a statistical ensemble of molecular trajectories from the FC state to the $S_1 \rightarrow S_0$ CInt was shown to enable quantitative prediction of the outstanding value of the isomerisation QY.[25,27] Here, we have focussed on describing the excited state PES topography and electronic character as well as the branching plane motions of **1**. Since the details of the trajectory actually followed by the system through the CInt region are required but still missing, this is not enough to provide a univocal rationalisation of the observed photo-isomerisation QY. However, we demonstrate and rationalise how electronic structures may be engineered to tune qualitatively and, in principle, continuously the nature of the molecular motions – *i.e.* from precessional to axial rotary motion – which ultimately governs the S_1 decay at the CInt.

Conclusions

The full disclosure of a mechanistic thread connecting apparently similar photoactuators, in particular rotary motors, remains a challenge. Taking inspiration from Nature and biomimetic switches, the introduction of electronic push–pull substituents in **1** is shown (i) to increase the quantum efficiency of the isomerisation process four-fold compared to the previous oxindole motors design, (ii) to maintain the positive features associated to oxindole motors, *i.e.* the synthetic accessibility and the visible light addressability, and (iii) to demonstrate a rationalised strategy for tuning the nature of the motion governing the S_1 decay at the CInt.

In conclusion, while motor **1** cannot yet be categorised as a genuine biomimetic scaffold, it exploits some attributes derived from natural photoswitches, such as engineered electronic effects to tune adequately the critical molecular motions driving the excited state decay and possibly improve the QY. Although the system itself is still far from reaching the QYs of Rho or the biomimetic switches, it paves the way to new structures aiming to go beyond the present push–pull design.

Author contributions

MO and BLF designed the study. DRSP synthesised the compounds investigated, performed NMR and steady-state UV-Vis experiments. RP and JL performed transient absorption data acquisition and analysis. SC performed quantum chemical calculations, CD measurements, part of the steady-state UV-Vis, and NMR experiments, quantum yield determination and related analysis. RC purified the enantiomers of the compounds investigated. LP performed the X-Ray measurements and analysed the data. MO, JL and BLF supervised the work. SC, DRSP and JL wrote the paper. All authors discussed and commented on the manuscript. SC, JL, MO, LP and BLF acquired funding.

Conflicts of interest

The authors declare there to be no conflicts of interest.

References

1 G. Wald, *Nature*, 1968, **219**, 800–807.
2 B. L. Feringa, *Angew. Chem., Int. Ed.*, 2017, **56**, 11060–11078.
3 W. R. Browne and B. L. Feringa, *Nat. Nanotechnol.*, 2006, **1**, 25–35.
4 M. Schildhauer, F. Rott, S. Thumser, P. Mayer, R. de Vivie-Riedle and H. Dube, *ChemPhotoChem*, 2019, **3**, 365–371.
5 R. Wilcken, M. Schildhauer, F. Rott, L. A. Huber, M. Guentner, S. Thumser, K. Hoffmann, S. Oesterling, R. de Vivie-Riedle, E. Riedle and H. Dube, *J. Am. Chem. Soc.*, 2018, **140**, 5311–5318.
6 R. Wilcken, L. Huber, K. Grill, M. Guentner, M. Schildhauer, S. Thumser, E. Riedle and H. Dube, *Chem.–Eur. J.*, 2020, **26**, 13507–13512.
7 V. Balzani, A. Credi and M. Venturi, *Chem. Soc. Rev.*, 2009, **38**, 1542–1550.
8 S. Kassem, T. Van Leeuwen, A. S. Lubbe, M. R. Wilson, B. L. Feringa and D. A. Leigh, *Chem. Soc. Rev.*, 2017, **46**, 2592–2621.
9 S. Gozem, F. Melaccio, H. L. Luk, S. Rinaldi and M. Olivucci, *Chem. Soc. Rev.*, 2014, **43**, 4019–4036.
10 D. Dattler, G. Fuks, J. Heiser, E. Moulin, A. Perrot, X. Yao and N. Giuseppone, *Chem. Rev.*, 2020, **120**, 310–433.
11 L. Greb and J. M. Lehn, *J. Am. Chem. Soc.*, 2014, **136**, 13114–13117.
12 C. J. Bruns and J. F. Stoddart, *The Nature of the Mechanical Bond*, John Wiley & Sons, Inc., Hoboken, NJ, USA, 2016.
13 M. Baroncini, S. Silvi and A. Credi, *Chem. Rev.*, 2020, **120**, 200–268.
14 M. Guentner, M. Schildhauer, S. Thumser, P. Mayer, D. Stephenson, P. J. Mayer and H. Dube, *Nat. Commun.*, 2015, **6**, 8406.

15 R. Schoenlein, L. Peteanu, R. Mathies and C. Shank, *Science*, 1991, **254**, 412–415.

16 H. J. A. Dartnall, *Vision Research*, 1968, **8**, 339–358.

17 S. Gozem, H. L. Luk, I. Schapiro and M. Olivucci, *Chem. Rev.*, 2017, **117**, 13502–13565.

18 Q. Wang, R. Schoenlein, L. Peteanu, R. Mathies and C. Shank, *Science*, 1994, **266**, 422–424.

19 D. W. McCamant, P. Kukura and R. A. Mathies, *J. Phys. Chem. B*, 2005, **109**, 10449–10457.

20 D. W. McCamant, *J. Phys. Chem. B*, 2011, **115**, 9299–9305.

21 D. Polli, P. Altoè, O. Weingart, K. M. Spillane, C. Manzoni, D. Brida, G. Tomasello, G. Orlandi, P. Kukura, R. A. Mathies, M. Garavelli and G. Cerullo, *Nature*, 2010, **467**, 440–443.

22 C. Schnedermann, M. Liebel and P. Kukura, *J. Am. Chem. Soc.*, 2015, **137**, 2886–2891.

23 P. J. M. Johnson, A. Halpin, T. Morizumi, V. I. Prokhorenko, O. P. Ernst and R. J. D. Miller, *Nat. Chem.*, 2015, **7**, 980–986.

24 B. G. Levine and T. J. Martínez, *Annu. Rev. Phys. Chem.*, 2007, **58**, 613–634.

25 I. Schapiro, M. N. Ryazantsev, L. M. Frutos, N. Ferré, R. Lindh and M. Olivucci, *J. Am. Chem. Soc.*, 2011, **133**, 3354–3364.

26 S. Hahn and G. Stock, *J. Phys. Chem. B*, 2000, **104**, 1146–1149.

27 C. Schnedermann, X. Yang, M. Liebel, K. M. Spillane, J. Lugtenburg, I. Fernández, A. Valentini, I. Schapiro, M. Olivucci, P. Kukura and R. A. Mathies, *Nat. Chem.*, 2018, **10**, 449–455.

28 *Molecular Switches*, ed. B. L. Feringa and W. R. Browne, Wiley-VCH Verlag GmbH & Co. KGaA, Weinheim, Germany, 2011.

29 C. Pezzato, C. Cheng, J. F. Stoddart and R. D. Astumian, *Chem. Soc. Rev.*, 2017, **46**, 5491–5507.

30 M. Kathan and S. Hecht, *Chem. Soc. Rev.*, 2017, **46**, 5536–5550.

31 Q. Li, G. Fuks, E. Moulin, M. Maaloum, M. Rawiso, I. Kulic, J. T. Foy and N. Giuseppone, *Nat. Nanotechnol.*, 2015, **10**, 161–165.

32 J. Michl and E. C. H. Sykes, *ACS Nano*, 2009, **3**, 1042–1048.

33 M. Filatov and M. Olivucci, *J. Org. Chem.*, 2014, **79**, 3587–3600.

34 D. Roke, S. J. Wezenberg and B. L. Feringa, *Proc. Natl. Acad. Sci. U. S. A.*, 2018, **115**, 9423–9431.

35 R. D. Astumian, *Chem. Sci.*, 2017, **8**, 840–845.

36 J. Chen, F. K. C. Leung, M. C. A. Stuart, T. Kajitani, T. Fukushima, E. Van Der Giessen and B. L. Feringa, *Nat. Chem.*, 2018, **10**, 132–138.

37 F. K. C. Leung, T. Van Den Enk, T. Kajitani, J. Chen, M. C. A. Stuart, J. Kuipers, T. Fukushima and B. L. Feringa, *J. Am. Chem. Soc.*, 2018, **140**, 17724–17733.

38 J. T. Foy, Q. Li, A. Goujon, J. R. Colard-Itté, G. Fuks, E. Moulin, O. Schiffmann, D. Dattler, D. P. Funeriu and N. Giuseppone, *Nat. Nanotechnol.*, 2017, **12**, 540–545.

39 R. Eelkema, M. M. Pollard, J. Vicario, N. Katsonis, B. S. Ramon, C. W. M. Bastiaansen, D. J. Broer and B. L. Feringa, *Nature*, 2006, **440**, 163.

40 D. Bléger, *Macromol. Chem. Phys.*, 2016, **217**, 189–198.

41 F. Lancia, A. Ryabchun and N. Katsonis, *Nat. Rev. Chem.*, 2019, **3**, 536–551.

42 A. Credi, M. Venturi and V. Balzani, *ChemPhysChem*, 2010, **11**, 3398–3403.

43 R. J. D. Miller, *Nat. Chem.*, 2012, **4**, 523–525.

44 F. Lumento, V. Zanirato, S. Fusi, E. Busi, L. Latterini, F. Elisei, A. Sinicropi, T. Andruniów, N. Ferré, R. Basosi and M. Olivucci, *Angew. Chem., Int. Ed.*, 2007, **46**, 414–420.

45 A. Melloni, R. R. Paccani, D. Donati, V. Zanirato, A. Sinicropi, M. L. Parisi, E. Martin, M. Ryazantsev, W. J. Ding, L. M. Frutos, R. Basosi, S. Fusi, L. Latterini, N. Ferre and M. Olivucci, *J. Am. Chem. Soc.*, 2010, **132**, 9310–9319.

46 M. Gueye, M. Manathunga, D. Agathangelou, Y. Orozco, M. Paolino, S. Fusi, S. Haacke, M. Olivucci and J. Léonard, *Nat. Commun.*, 2018, **9**, 313.

47 J. Léonard, I. Schapiro, J. Briand, S. Fusi, R. R. Paccani, M. Olivucci and S. Haacke, *Chem.–Eur. J.*, 2012, **18**, 15296–15304.

48 M. Gueye, M. Paolino, E. Gindensperger, S. Haacke, M. Olivucci and J. Léonard, *Faraday Discuss.*, 2020, **221**, 299–321.

49 I. V. Rubtsov and K. Yoshihara, *J. Phys. Chem. A*, 1999, **103**, 10202–10212.

50 M. Paolino, M. Gueye, E. Pieri, M. Manathunga, S. Fusi, A. Cappelli, L. Latterini, D. Pannacci, M. Filatov, J. Léonard and M. Olivucci, *J. Am. Chem. Soc.*, 2016, **138**, 9807–9825.

51 C. McLaughlin, M. Assmann, M. A. Parkes, J. L. Woodhouse, R. Lewin, H. C. Hailes, G. A. Worth and H. H. Fielding, *Chem. Sci.*, 2017, **8**, 1621–1630.

52 D. Roke, M. Sen, W. Danowski, S. J. Wezenberg and B. L. Feringa, *J. Am. Chem. Soc.*, 2019, **141**, 7622–7627.

53 A. Nikiforov, J. A. Gamez, W. Thiel and M. Filatov, *J. Phys. Chem. Lett.*, 2016, **7**, 105–110.

54 J. Wang and B. Durbeej, *ChemistryOpen*, 2018, **7**, 583–589.

55 G. Marchand, J. Eng, I. Schapiro, A. Valentini, L. M. Frutos, E. Pieri, M. Olivucci, J. Léonard and E. Gindensperger, *J. Phys. Chem. Lett.*, 2015, **6**, 599–604.

56 I. Schapiro, M. Gueye, M. Paolino, S. Fusi, G. Marchand, S. Haacke, M. E. Martin, M. Huntress, V. P. Vysotskiy, V. Veryazov, J. Léonard and M. Olivucci, *Photochem. Photobiol. Sci.*, 2019, **18**, 2259–2269.

57 M. Paolino, T. Giovannini, M. Manathunga, L. Latterini, G. Zampini, R. Pierron, J. Léonard, S. Fusi, G. Giorgi, G. Giuliani, A. Cappelli, C. Cappelli and M. Olivucci, *J. Phys. Chem. Lett.*, 2021, 3875–3884.

58 N. Koumura, R. W. J. Zijistra, R. A. Van Delden, N. Harada and B. L. Feringa, *Nature*, 1999, **401**, 152–155.

59 I. Schapiro, F. Melaccio, E. N. Laricheva and M. Olivucci, *Photochem. Photobiol. Sci.*, 2011, **10**, 867.

60 J. Conyard, K. Addison, I. A. Heisler, A. Cnossen, W. R. Browne, B. L. Feringa and S. R. Meech, *Nat. Chem.*, 2012, **4**, 547–551.

61 M. N. G. James and G. J. B. Williams, *Can. J. Chem.*, 1972, **50**, 2407–2412.

62 K. Stranius and K. Börjesson, *Sci. Rep.*, 2017, **7**, 41145.

63 J. Otsuki, K. Suwa, K. K. Sarker and C. Sinha, *J. Phys. Chem. A*, 2007, **111**, 1403–1409.

64 *Molecular Switches*, ed. B. L. Feringa and W. R. Browne, Wiley-VCH Verlag GmbH & Co. KGaA, Weinheim, Germany, 2011.

65 M. L. Horng, J. A. Gardecki, A. Papazyan and M. Maroncelli, *J. Phys. Chem.*, 1995, **99**, 17311–17337.

66 J. Briand, O. Bräm, J. Réhault, J. Léonard, A. Cannizzo, M. Chergui, V. Zanirato, M. Olivucci, J. Helbing and S. Haacke, *Phys. Chem. Chem. Phys.*, 2010, **12**, 3178.

67 H. Barkhuijsen, R. de Beer, W. M. M. Bovée and D. van Ormondt, *J. Magn. Reson.*, 1985, **61**, 465–481.

68 H. Barkhuijsen, R. de Beer and D. van Ormondt, *J. Magn. Reson.*, 1986, **67**, 371–375.

69 A. L. Dobryakov, I. Ioffe, A. A. Granovsky, N. P. Ernsting and S. A. Kovalenko, *J. Chem. Phys.*, 2012, **137**, 244505.

70 M. Quick, F. Berndt, A. L. Dobryakov, I. N. Ioffe, A. A. Granovsky, C. Knie, R. Mahrwald, D. Lenoir, N. P. Ernsting and S. A. Kovalenko, *J. Phys. Chem. B*, 2014, **118**, 1389–1402.

71 S. Amirjalayer, A. Cnossen, W. R. Browne, B. L. Feringa, W. J. Buma and S. Woutersen, *J. Phys. Chem. A*, 2016, **120**, 8606–8612.

72 J. Conyard, A. Cnossen, W. R. Browne, B. L. Feringa and S. R. Meech, *J. Am. Chem. Soc.*, 2014, **136**, 9692–9700.

73 C. R. Hall, J. Conyard, I. A. Heisler, G. Jones, J. Frost, W. R. Browne, B. L. Feringa and S. R. Meech, *J. Am. Chem. Soc.*, 2017, **139**, 7408–7414.

74 I. F. Galván, M. G. Delcey, T. B. Pedersen, F. Aquilante and R. Lindh, *J. Chem. Theory Comput.*, 2016, **12**, 3636–3653.

75 I. N. Ioffe and A. A. Granovsky, *J. Chem. Theory Comput.*, 2013, **9**, 4973–4990.

76 L. Pfeifer, M. Scherübl, M. Fellert, W. Danowski, J. Cheng, J. Pol and B. L. Feringa, *Chem. Sci.*, 2019, **10**, 8768–8773.

77 P. Roy, A. S. Sardjan, A. Cnossen, W. R. Browne, B. L. Feringa and S. R. Meech, *J. Phys. Chem. Lett.*, 2021, **12**, 3367–3372.

78 J. Saltiel and S. Gupta, *J. Phys. Chem. A*, 2018, **122**, 6089–6099.

79 A. Kazaryan, Z. Lan, L. V. Schäfer, W. Thiel and M. Filatov, *J. Chem. Theory Comput.*, 2011, **7**, 2189–2199.

80 M. Quick, A. L. Dobryakov, I. N. Ioffe, A. A. Granovsky, S. A. Kovalenko and N. P. Ernsting, *J. Phys. Chem. Lett.*, 2016, **7**, 4047–4052.

81 J. Saltiel, *J. Am. Chem. Soc.*, 1967, **89**, 1036–1037.

82 C. R. Hall, W. R. Browne, B. L. Feringa and S. R. Meech, *Angew. Chem., Int. Ed.*, 2018, **57**, 6203–6207.

83 N. Minezawa and M. S. Gordon, *J. Phys. Chem. A*, 2011, **115**, 7901–7911.